CrossMark

Catalytic removal of chlorinated compounds over ordered mesoporous cobalt oxides synthesised by hard-templating

J. González-Prior, R. López-Fonseca, J.I. Gutiérrez-Ortiz, B. de Rivas*

Chemical Technologies for Environmental Sustainability Group, Department of Chemical Engineering, Faculty of Science and Technology, University of The Basque Country (UPV/EHU), PO Box 644, E-48080 Bilbao, Spain

ARTICLE INFO

ABSTRACT

This work evaluates the catalytic behaviour of a series of mesoporous bulk cobalt oxide prepared by hard-templating using SBA-15, SBA-16 and SBA-3. In addition, a bulk catalyst obtained by silica aquagel confined precipitation is also examined. The oxidation of 1,2-dichloroethane has been selected as a model reaction for determining their suitability for the efficient removal of chlorinated pollutants in gaseous waste streams.

The catalytic behaviour is found to depend on the abundance of surface adsorbed oxygen species and a good low-temperature reducibility. These key physico-chemical properties are optimised for nanocasted Co_3O_4 prepared by using SBA-15 as hard template. This sample is characterised by a relatively high surface area, a nanorod-like morphology and a high quality 2D ordered mesoporous structure. At 375–400 °C this sample attains an efficient oxidation of the chlorinated feed to CO_2 and HCl/Cl_2 while keeping a reasonable stability with time.

1. Introduction

Chlorinated organic compounds, which are emitted from a wide range of industrial processes, such as polymer synthesis and processing, production of pesticides, solvents, insulators or electronic devices, are linked with the formation of low-level ozone and photochemical smog, stratospheric ozone depletion, and are considered greenhouse gases. Catalytic combustion is accepted as an attractive technology for removal at low temperatures when operating with dilute effluent streams. The proper catalyst selection and subsequent optimisation are essential for achieving efficient oxidation.

In order to avoid the use of noble metals in the catalyst formulation, substantial efforts have made in the design of suitable alternatives in terms of activity and cost. In this sense, much interest has been given to the development of Co_3O_4-based catalysts due to their notable performance in comparison with other transition metal oxides [1,2]. The catalytic activity of Co_3O_4 is essentially related to its surface area, pore structure, oxygen nonstoichiometry, and reducibility [3]. These properties in turn are intimately related to the surface morphology and the exposed crystal planes of the spinel. All these physico-chemical features can be optimised by the preparation method [4,5].

As an alternative to conventional and soft-templating synthesis routes, the hard-templating method is an attractive route for the synthesis of mesoporous Co_3O_4. Ordered mesopores silica is especially adequate as solid template for obtaining structured materials owing to

its highly tailorable textural properties [6]. In addition to leading to bulk catalysts with a relatively high surface area and a controllable pore structure, which are derived from replication of the pore system of the template, the nanomorphology can be tuned. Besides the channels of the template may induce a positive confinement effect on the predominantly exposed planes [7,8].

The objective of this work is the synthesis, characterisation and evaluation of a series of mesoporous bulk cobalt oxide catalysts for the oxidation of 1,2-dichloroethane ($C_2H_4Cl_2$, DCE), which has been chosen as a model chlorinated pollutant. More particularly, the effect of the selection of the silica template (SBA-15, SBA16 and SBA-3) on the physico-chemical properties of the nanocasted Co_3O_4 has been analysed.

2. Experimental

2.1. Template preparation

Three different silicas, namely SBA-15, SBA-3 and SBA-16, were synthesised and subsequently used as hard-templates for the preparation of Co_3O_4 catalysts. The SBA-15 and SBA-3 are mesoporous silicas templates with a two-dimensional p6 mm cubic arrangement of pores. SBA-15 shows hexagonal pores in a 2D array with long 1D channels (p6 mm plane group). The channels are interconnected by small micropores. SBA-3 has a uniformly ordered pore structure with a linear

channel array of mesopores, with a 2D hexagonal structure. The SBA-16 matrix is a material with a 3D cubic arrangement of mesopores corresponding to the Im3 m space group. Each mesopore in this body-centred cubic structure is connected with its eight nearest neighbors. These materials were prepared according to the synthesis procedures described in the literature, namely SBA-15 [9,10] and SBA-3 and SBA-16 [5,11].

2.2. Synthesis of hard-templated samples

Using these three silicas as templates (SBA-15, SBA-3 and SBA-16), different Co_3O_4 catalysts were prepared by means of wet impregnation method under reduced pressure using a rotary evaporator. An aqueous solution (100 cm^3) of cobalt (II) nitrate was used, with a Co/Si molar ratio of 0.25. In an attempt to examine the effect of this parameter, the SBA-15 silica was also impregnated with a more concentrated aqueous solution, with a Co/Si molar ratio of 0.4. In this case, the pores of the silica were expected to be completely filled and some cobalt oxide were likely formed out of the silica structure. This was confirmed by the notable decrease in surface area observed for this sample (320 $m^2 g^{-1}$) in comparison with that of the impregnated sample with a lower Co/Si molar ratio (440 $m^2 g^{-1}$). On the other hand, an additional cobalt oxide catalyst was prepared by silica aquagel confined coprecipitation (the so-called SACOP method). Thus, the precursor of the metal oxide was introduced in the cast during the synthesis step of the silica. The catalyst was obtained by mixing sodium silicate, hydrochloric acid, distilled water and cobalt nitrate hexahydrate with a $SiO_2/Co/H^+/H_2O$ molar ratio of 1/0.25/6.54/193.9 for 24 h. Then, the mixture was transferred to an autoclave under hydrothermal conditions at 100 °C for additional 24 h. Next, the metal hydroxide was precipitated with NaOH 3.5 mol L^{-1}. Finally, the solid was washed, dried and calcined at 500 °C [12].

Finally, once the cobalt oxide was inside the pores of the various silicas, the matrix was removed using NaOH 2 mol L^{-1}. This step was repeated four times allowing for obtaining nanocasted pure cobalt oxide. All samples were then washed several times with distilled water to remove the remaining NaOH and then dried at 110 °C overnight. Thus, the Co-S15 sample was obtained from the cobalt oxide impregnated on the SBA-15 silica. When using a higher Co/Si molar ratio (0.4) the sample was labelled as Co-S15(0.4). Similarly, the Co-S3 and Co-S16 oxides were prepared using SBA-3 and SBA-16 silicas, respectively while the Co-SP oxide was the sample synthesised by the SACOP method.

2.3. Characterisation techniques

Textural properties were evaluated from the nitrogen adsorption-desorption isotherms, determined at −196 °C with a Micromeritics TRISTAR II apparatus. The specific surface areas of the samples were determined in line with standard BET procedure. The mean pore size was calculated using the BJH method. The samples were previously degassed overnight with N_2 flow.

X-ray diffraction (XRD) studies were carried out on a X'PERT-MPD X-ray diffractometer with Cu Kα radiation (λ = 1.5406 Å) and Ni filter. The X-ray tube was operated at 30 kV and 20 mA. Samples were scanned from 5° < 2θ < 80° and the X-ray diffraction line positions were determined with a step size of 0.02° and counting time of 2.5 s per step. Phase identification was conducted by comparison with ICDD (International Centre for Diffraction Data) database cards.

Transmission electron microscopy (TEM) investigations were performed using a Philips CM200 microscope equipped with LaB6 crystal as electron source and operating at 200 kV. Bright field images were acquired using a high resolution CCD camera. Drops of emulsions, created by sonication of the powder samples in ethanol, were deposited on C coated Cu grids and left in air to dry. HRTEM measurements were carried out with a FEI Titan Cubed G2 60–300 electron microscope at

300 kV equipped with a high-brightness X-FEG Schottky field emission electron gun and a monochromator and CEOS GmbH spherical aberration (Cs) corrector on the image side. The images were recorded on a charge-coupled device (CCD) camera (2kx2k Gatan UltraScanTM 1000). The sample was prepared by dispersion into ethanol solvent and keeping the suspension in an ultrasonic bath for 15 min, after a drop of suspension was spread onto a TEM copper grid (300 mesh) covered by a holey carbon film followed by drying under vacuum.

X-ray photoelectron spectroscopy studies were performed using in a SPECS system with equipped with Phoibos 150 1D analyzer and DLD-monochromatic radiation source.

The IR spectra were recorded on a Thermo Scientific Nicolet 380 FT-IR spectrometer in the range of 4000–400 cm^{-1}. The skeletal characterization was carried out diluting 1 mg of each powder with 100 mg of IR-grade KBr powder finely mixed in an agate mortar and subjected to a pressure of 2 ton to obtain suitable self-supporting disks for the IR analysis.

Redox behaviour was examined by temperature-programmed reduction experiments (TPR) with hydrogen. These experiments were conducted on a Micromeritics Autochem 2920 instrument. Firstly, all the samples (20 mg) were pre-treated in an oxygen stream (5%O_2/He) at 400 °C for 1 h, and then cooled down to room temperature. The reducing gas used in all experiments was 5%H_2 in Ar, with a flow rate of 50 $cm^3 min^{-1}$. The temperature range explored was from room temperature to 600 °C with a heating rate of 10 °C min^{-1}. This temperature was held for 0.5 h. The water produced by the reduction process was trapped into a cold trap. The consumption of H_2 was quantitatively measured by time integration of TPR profiles. The calibration sample for quantitative analysis of H_2 uptake was silver oxide.

The total acidity of the catalysts was evaluated by NH_3 adsorption at 100 °C followed by thermogravimetry. These experiments were carried out with a Setaram Setsys Evolution thermobalance under atmospheric pressure coupled to a Pfeiffer Prisma mass spectrometer. Prior to adsorption experiments, the samples were first pretreated in a helium stream at 500 °C (10 °C min^{-1}) and then cooled to 100 °C (40 °C min^{-1}). Later, the NH_3 adsorption step was performed by admitting a flow of 10% NH_3/He at 100 °C up to saturation. Subsequently, the samples were exposed to a flow of helium (50 $cm^3 min^{-1}$) for 2 h at 100 °C to remove reversibly and physically bound ammonia from the surface. The mass variation and the sample temperature were continuously recorded by a computerised data acquisition system. The net weight gain was considered as the total acidity of the samples. Then, the temperature was increased from 100 to 500 °C at a constant heating rate of 10 °C min^{-1}. The exit stream was analysed by on-line mass spectrometry.

2.4. Catalyst activity determination

Catalytic tests were performed in a bench-scale fixed bed reactor (Microactivity modular laboratory system provided by PID Eng & Tech S.L.) operated at atmospheric pressure and fully monitored by computer. The reactor is made of quartz with an internal diameter of 10 mm and a height of 300 mm, in which the temperature is measured with a thermocouple placed in the catalyst bed. Typically, 0.85 g of catalyst in powdered form (0.3–0.5 mm) was loaded. No quartz sands mixed with the catalyst were used. The reaction feed consisted of 1000 ppm of DCE in dry air with a total gas flow of 500 $cm^3 min^{-1}$. The corresponding gas hourly space velocity was 30,000 h^{-1}. The amount and particle size of catalyst and the total gas flow rate were chosen in order to be out of the internal and external diffusion limits. Catalytic activity was measured over the range 150–500 °C and conversion data were calculated by the difference between inlet and outlet concentrations. Conversion measurements and product profiles were taken at steady state, typically after 30 min on stream. Either product selectivity was calculated based on either chlorine or carbon atoms present in that product divided by the total chlorine or carbon atoms present in the product stream

Table 1
Textural and structural properties of the hard-templated Co_3O_4 samples.

Catalyst	BET surface area, $m^2 g^{-1}$	Pore volume, $cm^3 g^{-1}$	Maxima in the pore size distribution, Å	Crystallite size, nm	Amount of residual SiO_2, %	Total acidity, mmol $NH_3 g^{-1}$	Acid density, mmol $NH_3 m^{-2}$
SBA-3	257	0.68	125	–	–	–	
SBA-15	749	0.71	39	–	–	–	
SBA-16	785	0.61	39	–	–	–	
Co-S15	83	0.18	35	16	2.3	0.46	$5.5 \cdot 10^{-3}$
Co-S3	53	0.25	160/232	26	1.2	0.31	$5.8 \cdot 10^{-3}$
Co-S16	123	0.26	53/62	12	3.6	0.54	$4.4 \cdot 10^{-3}$
Co-SP	111	0.18	35/62	13	6.9	0.29	$2.6 \cdot 10^{-3}$
Co-S15(0.4)	62	0.13	35	29	1.6	0.30	$4.8 \cdot 10^{-3}$

(expressed as%). The feed and effluent stream were analysed using an on-line 7980A Agilent Technologies gas chromatograph equipped with a thermal conductivity detector (CO and CO_2) and an electron capture detector (chlorinated hydrocarbons). Analysis of HCl and Cl_2 was carried out by means of ion selective electrode and titration, respectively. Further details on analytical procedures are described elsewhere [13].

3. Results

3.1. Characterisation of the hard-templated Co_3O_4 catalysts

The textural properties of the synthesised silicas used as hard templates were previously examined. Their BET surface area, pore volume and average pore size are summarised in Table 1. The corresponding N_2 physisorption isotherms and pore size distribution are included in Figs. S1 and S2 (supplementary material). The SBA-3 silica exhibited a noticeable lower surface about 260 $m^2 g^{-1}$ in comparison with that exhibited by both SBA-15 and SBA-16 materials, with a surface area of 750 and 785 $m^2 g^{-1}$, respectively. The three samples presented a type IV isotherm. In this sense, an ordered mesoporous structure of these siliceous materials was directly evidenced by TEM (Fig. 1). The N_2 isotherm of SBA-16, with a broad H2-type hysteresis loop and a unimodal pore size distribution at 39 Å, was comparable to that reported in the literature [14]. However, the expected well-defined H1-type hysteresis loop with almost vertical and parallel adsorption-desorption branches was not obtained for the as-synthesised SBA-15, probably due its non-uniform pore size pore size distribution [15]. Note that, in addition to a main peak centred at 39 Å, a shoulder at around 56 Å was also observed. On the other hand, a much larger pore size of 125 Å (typically 30 Å for this kind of materials), and consequently a markedly low surface area were found for SBA-3 [16]. This was probably due to the high CTAB:TEOS molar ratio (3.6) used in the synthesis (supplementary material).

A set of hard templated cobalt oxide catalysts were obtained after impregnation followed by calcination and subsequent silica removal with sodium hydroxide. Results included in Table 1 pointed out that

small amounts of SiO_2 between 1.2 and 3.6 wt% were still presented in the Co-S3, Co-S15(0.4), Co-S15 and Co-S16 catalysts. The presence of residual silica was in agreement with the results given by other authors who pointed out that the remaining silica was very likely trapped among the crystallites of Co_3O_4 [17,18]. However, a relatively higher amount of SiO_2 close to 7 wt% was found in the case of the Co-SP sample. Hence, the dissolution of silica with NaOH was considerably less efficient for such sample. In agreement with the previous results, TEM analysis coupled to EDX clearly identified the presence of silica particles (Fig. S3, supplementary material). On the other hand, no analysis of the used NaOH aqueous solution was carried to check the eventual dissolution of cobalt species.

The structural properties were characterised by XRD using the ICDD files as a reference. Fig. 2 shows the XRD patterns of the five samples calcined at 500 °C. For every catalyst all the reflection peaks, located at 2θ 19°, 31.3°, 36.8°, 44.8°, 59.3° and 65.2°, could be assigned to a pure cubic phase of cobalt (II,III) oxide spinel (PDF 42–1467), irrespectively of the used hard template. No diffraction peaks related to a CoO phase were detected. The average Co_3O_4 crystallite diameters, estimated from the full width at half maximum of the characteristic diffraction peaks by applying the Scherrer equation (Table 1), ranged between 12 and 16 nm for the Co-S15, Co-S16 and Co-SP samples, while a larger crystallite size was found for the Co-S3 and Co-S15(0.4) samples (26 and 29 nm, respectively).

Fig. 3 includes the TEM images of the as-prepared Co_3O_4 samples after the silica removal. 2D highly ordered mesoporous architectures were found in the two SBA-15-derived bulk catalysts (Fig. 3a and e). This was probably connected to the fullfilling of the mesopores of the silica matrix with the aqueous solution of cobalt nitrate irrespective of the used Co/Si ratio. As a result, rod-like structures were assumed to be formed inside the silica pores, thereby promoting the crystallite growth with the same shape as the pores. Interestingly, after the silica removal these morphologies still remained, being reasonable replicas of this silica template. By contrast, a 3D wormhole-like mesoporous structure was noticed for the Co-S3 and Co-S16 catalysts (Fig. 3b and c, respectively) presumably due to an incomplete coverage of the mesopores or
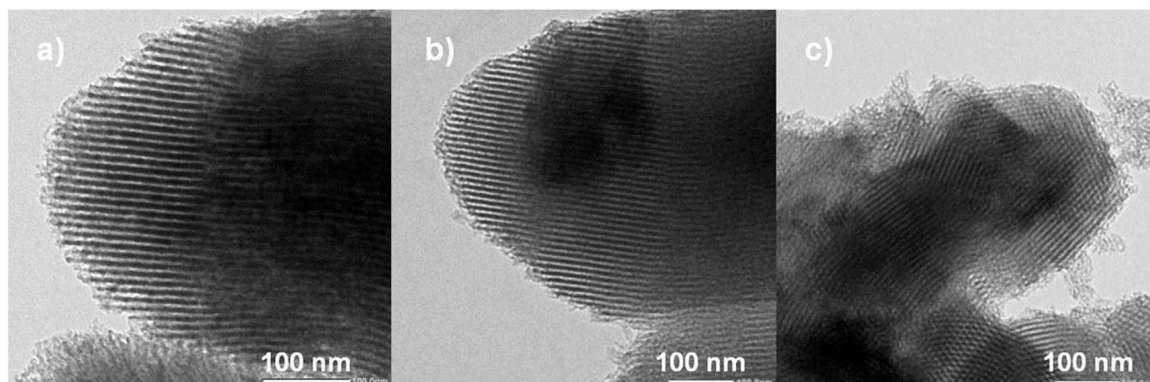

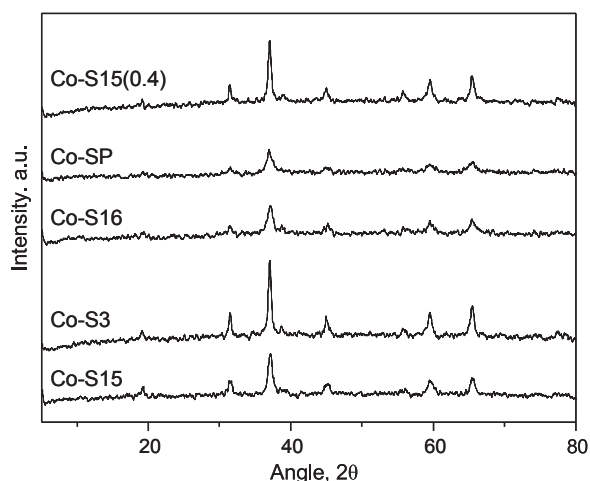**Fig. 1.** TEM images of silica templates: a) SBA-3, b) SBA-15, c) SBA-16.

Fig. 2. XRD patterns of the hard-templated Co_3O_4 samples.

the loss of the structure when the cobalt precursor was incorporated [19,20]. Finally, it must be pointed out that the morphology of the Co-SP sample (Fig. 3d) was a mixture of both ordered and wormhole-like structures. These results contrast with those found by Lopez et al. [10] who observed a needle-shaped nanostructure for this type of material.

This different morphology could be related to the lower calcination temperature (400 °C) in comparison with 500 °C used in this work.

The textural properties in terms of BET surface area, pore volume and average pore size of the Co_3O_4 catalysts are shown in Table 1. The corresponding N_2 physisorption isotherms of the hard-templated samples are depicted in Fig. S4 (supplementary material). Except for the Co-S3 sample the surface areas of the ordered rods were noticeably lower (62–83 $m^2\,g^{-1}$) than the wormhole-like structures (111–123 $m^2\,g^{-1}$) [19]. It must be pointed out that the contribution of residual silica to the surface area of the samples, while assuming that its original textural properties were preserved after the treatment with NaOH solution, was about 20% (5% for the Co-S3 catalyst). The pore size distribution shown in Fig. S5 (supplementary material) also revealed noticeable differences among the synthesised mesoporous materials. Thus, when the SBA-15 silica was used, irrespective of the Co/Si ratio, a unimodal pore distribution was noted with a peak centred at around 35 Å. The mesopores of these samples were formed via the 2D connections of Co_3O_4 skeletons. In the case of Co-S16 a wide pore distribution was found as well but with a slightly larger average size. Thus, the maximum values were located at 53 and 62 Å. On the other hand, when using the SACOP method and the SBA-3 template, the resulting oxides displayed a clear bimodal pore distribution. The Co-SP sample presented pores of a similar size to the other samples, centred at 35 and 62 Å, whereas the Co-S3 sample exhibited comparatively much larger pore sizes with peaks located at 160 and 232 Å. The wider pore distribution and consequently
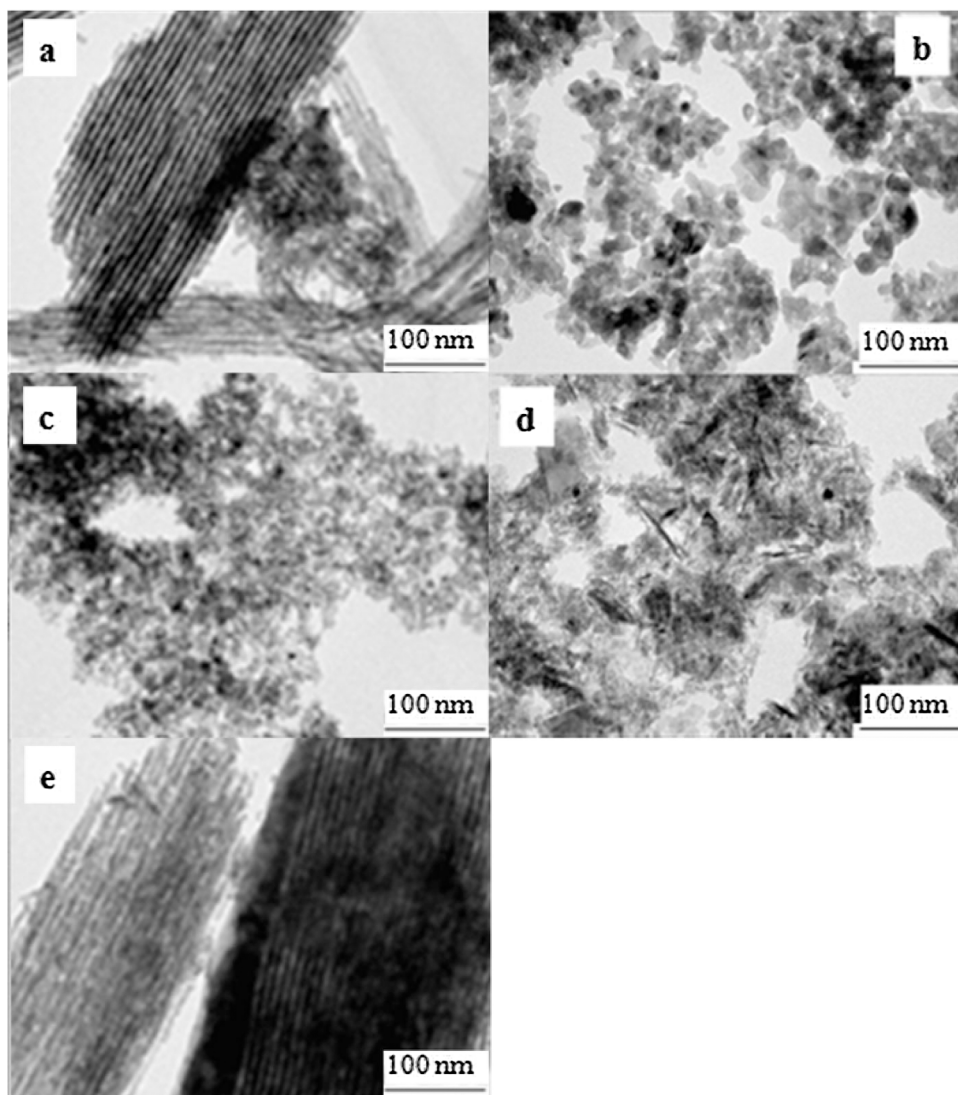
Fig. 3. TEM images of the hard-templated Co_3O_4 samples: a) Co-S15, b) Co-S3, c) Co-S16, d) Co-SP, e) Co-S15(0.4).
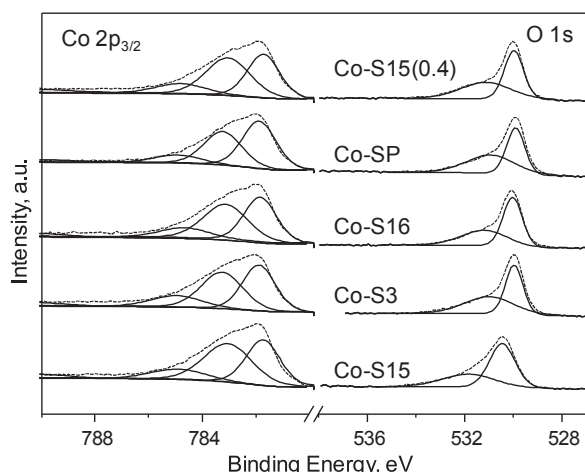
Fig. 4. O 1s and Co 2p$^{3/2}$ XPS spectra of the hard-templated Co_3O_4 samples.

Fig. 5. Redox behaviour of the hard-templated Co_3O_4 samples.

the larger average pore size suggested that the mesopores of the Co-S16, Co-S3 and Co-SP oxides were originated from the irregular compiling of Co_3O_4 nanoparticles.

XPS analysis was employed to gain further insight into the surface composition, metal oxidation state, and adsorbed species of the prepared bulk oxides. Fig. 4 illustrates the Co 2p$_{3/2}$ and O 1s XPS spectra of the cobalt catalysts. Hence, an asymmetrical Co 2p$_{3/2}$ peak, which could be decomposed into three components at a binding energy 779.2, 781.7 and 782.5 eV, was noticed. The first signal was assigned to the surface Co^{3+} species and the second one to surface Co^{2+} species, whereas the latter corresponded to the presence of CoO species on the surface [21]. The contribution of these species were estimated to be roughly similar on the five samples and around than 10–15% of the total amount of cobalt. The low intensity peaks that appeared at 785.4 and 790.0 eV were characteristic shake-up satellites of CoO and Co_3O_4, respectively [16]. On the other hand, by adopting the curve-fitting method, the asymmetrical O 1s XPS band of each sample could be decomposed into two components. The first signal located at 529.8 eV was attributable to the surface lattice oxygen (O_{latt}) species. The other peak (531 eV) was assigned to adsorbed oxygen (O_{ads} species as O^-, O^{2-} or O_2^{2-}) species [20,22]. Table 2 lists the quantitative analysis of the XPS spectra in terms of O_{ads}/O_{latt} and Co^{2+}/Co^{3+} ratios. These were calculated from the relative intensities of the corresponding peaks. A good relationship between surface Co^{2+} and oxygen species concentration was found, in agreement with [20]. The abundance of these species appreciably decreased according to the following order: Co-S15 > Co-S15(0.4) > Co-S16 > Co-S3 > Co-SP. This notable variation in surface Co^{2+}/Co^{3+} molar ratio, from 1.2 to 0.8, and surface O_{ads}/O_{latt} molar ratio, from 0.98 to 0.64, clearly evidenced that the synthesis method played an important role in determining the surface composition.

The redox properties of cobalt catalysts were investigated by temperature-programmed reduction with hydrogen. The profiles shown in
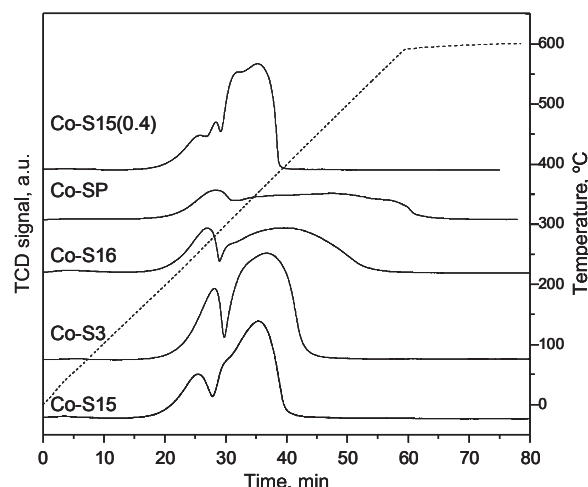
Fig. 5 varied appreciably from one sample to another, thus evidencing the existence of various reducible species [17,23]. In all cases the profile could be divided into two zones more or less discernible: one below 300 °C attributable to the reduction of Co_3O_4 to CoO and another one above this temperature related to the reduction of CoO to Co. This assignation was reasonable since the reduction of Co_3O_4 takes place according to the sequence of $Co_3O_4 \rightarrow CoO \rightarrow Co^0$, with an ideal H_2 uptake of 1:3. In view of the location of the reduction band at low temperatures, the oxygen mobility within the lattice could be indirectly ranked as follows: Co-S15 (250 °C) > Co-S16 (265 °C) > Co-S3 (275 °C) > Co-SP (285 °C). It should be pointed out that the low-temperatures reducibility occurred in a slightly wider temperature range (250–280 °C) over the Co-S15(0.4) sample. Therefore, the existence of a higher amount of oxygen defects (evidenced by a high surface Co^{2+}/Co^{3+} ratio) enhanced the oxygen mobility in the lattice as revealed by the promoted reduction at low temperature.

The reduction process of the samples occurred in the 200–525 °C window, but higher temperatures (600 °C) were required in the case of the Co-SP sample, thereby pointing out the formation of more stable CoO_x species. The degree of reduction of the samples was calculated based on the fact that 100% of cobalt is present as Co_3O_4. A quantitative evaluation of the amounts of hydrogen consumed during reduction (about 16.6 mmol H_2 g_{Co3O4}^{-1}) revealed that in all cases Co_3O_4 was converted into metallic cobalt completely, except for the Co-SP catalyst, which only reached a degree of reducibility of about 90%. This suggested the presence of cobalt species (presumably cobalt silicate) which were not reduced below 600 °C. In this sense, FT-IR studies were carried out to better analyse the skeletal structure of each sample (Fig. 6). Thus, the features due to the cobalt-oxygen vibrational modes of cobalt species could be clearly seen. These bands at around 565 and 661 cm^{-1} (with shoulders at higher frequencies) are typical of the Co_3O_4 spinel phase [9,24,25]. They correspond to vibrations of tetrahedral Co^{3+} and octahedral Co^{2+}, respectively, in the spinel structure. In addition, particularly in the Co-SP sample small bands in the 1200–800 cm^{-1} could be detected. The bands in this region are characteristic of silica-based materials. The broad peak centred at 1015 cm^{-1} was associated with the silica support not efficiently removed by NaOH. Moreover, the presence of a peak at around 890 cm^{-1} was assigned to vibrations mode in a cobalt silicate phase [26].

The overall acidity of the catalysts was evaluated from the net weight gain recorded after an isothermal adsorption step at 100 °C followed by removal of physisorbed ammonia with an inert stream (Table 1). It was found that the Co-S15 and Co-S16 oxides exhibited a higher total acidity, namely 0.46 and 0.54 mmol NH_3 g^{-1}, respectively, while the remaining three oxides were considerably less acidic, with an overall acidity close to 0.30 mmol NH_3 g^{-1}. The differences among the

Table 2
XPS surface composition and reducibility of the hard-templated Co_3O_4 samples.

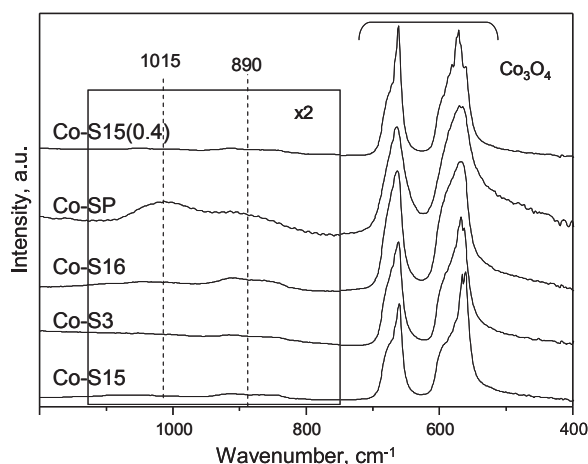| Catalyst	Surface O_{ads}/O_{latt}	Surface Co^{2+}/Co^{3+}	H$_2$ consumption	
			1 st peak, °C	2° peak, °C	%reduction
Co-S15	0.98	1.20	250	355, 300 sh	100
Co-S3	0.76	0.98	275	360, 320 sh	100
Co-S16	0.83	1.04	265	395, 300 sh	99
Co-SP	0.64	0.80	285	475	90
Co-S15(0.4)	0.91	1.16	250–280	310–355	100

sh: shoulder.

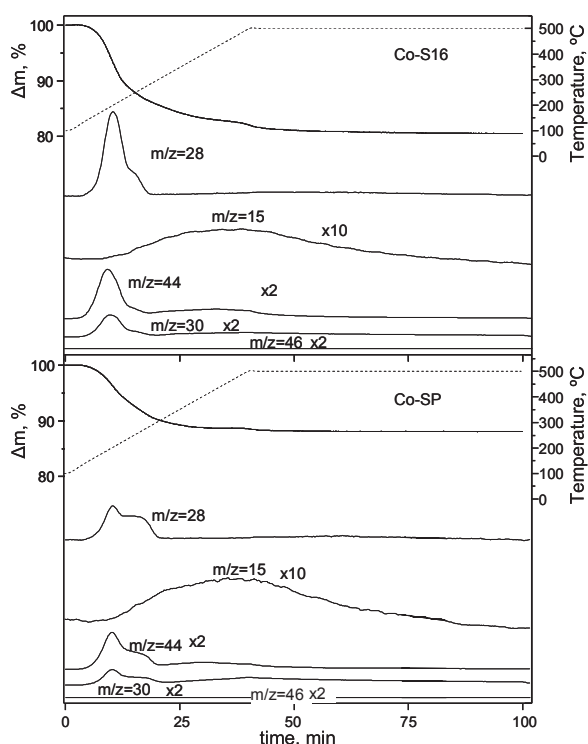**Fig. 6.** FT-IR skeletal spectra of the hard-templated Co_3O_4 samples.

Fig. 7. Temperature-programmed reaction of adsorbed ammonia followed by thermogravimetry coupled to mass spectrometry.

samples were less apparent when the acid density was compared, since this property varied between 4 and 6 mmol $NH_3\,m^{-2}$, except for the Co-SP sample, which exhibited a significantly lower value (2.6 mmol $NH_3\,m^{-2}$). The surface reactivity of the catalyst was examined by following the decomposition of this adsorbed probe molecule with increasing temperature under inert conditions. This analysis was carried out by a combined study of the evolution of the weight loss and the composition of the exit stream by mass spectrometry. This investigation could be helpful in evidencing the participation of the oxygen species present in the samples. As an example, the results corresponding to the Co-S16 and Co-SP catalysts are included in Fig. 7. These (m/z) MS signals were recorded, namely 15 (NH_3), 18 (H_2O), 28 (N_2), 30 (NO, N_2O or NO_2), 44 (N_2O) and 46 (NO_2). At relatively low temperatures the formation of N_2 ($m/z = 28$) was noticed as the main oxidation product ($4NH_3 + 3O_2 \rightarrow 2N_2 + 6H_2O$) [27]. Simultaneously, N_2O ($m/z = 44$) was detected ($2NH_3 + 2O_2 \rightarrow N_2O + 3H_2O$). Since the profile of this signal was identical in shape to that observed for the

($m/z = 30$) signal, the latter was also associated with the presence of N_2O. Accordingly, the presence of NO as oxidation product ($4NH_3 + 5O_2 \rightarrow 4NO + 6H_2O$), which could be also followed by the ($m/z = 30$) signal, was ruled out. The presence of NO_2 ($2NH_3 + 7O_2 \rightarrow 2NO_2 + 3H_2O$) was also negligible as the ($m/z = 46$) signal was flat. Above 300 °C only trace amounts of ammonia ($m/z = 15$) were detected, probably due to the fact that the active oxygen species were already consumed. Therefore, the unreacted ammonia was desorbed at higher temperatures. It must be stated that no marked differences were noticed in the behaviour of the Co-S15, Co-S16, Co-S3 and Co-S15(0.4) catalysts, since a similar evolution of the product distribution with temperature was noticed. Therefore, the oxidation of adsorbed ammonia was not suitable for identifying the most active catalyst for DCE, presumably owing to the high reactivity of NH_3. Only the Co-SP catalyst exhibited a somewhat lower activity as oxidation products were found at slightly higher temperatures on the basis of the wider temperature window in which N_2 and N_2O were detected. In addition, a favoured formation of N_2O instead of N_2, which occurred at around 300 °C, was noticed. This was related to its lower population of active oxidation sites at low temperatures. In the case of the other samples, N_2 was detected as the main oxidation product, with a comparable N_2/N_2O formation.

3.2. Behaviour of the hard-templated Co_3O_4 catalysts

The catalytic behaviour of the prepared samples was examined by analysing the evolution of the conversion of DCE to CO_2 with the temperature, which are shown in Fig. 8. The corresponding values of T_{50} and T_{90} are summarised in Table 3. The investigated bulk catalysts exhibited a reasonably good performance since in all cases the chlorinated feed was completely abated (100% conversion to CO_2) between 350 and 425 °C, thereby revealing that synthesis routes based on the use of silica as hard template were efficient. Indeed, when compared with our recent results on Co_3O_4 prepared via soft-templates [13], these required noticeably higher oxidation temperatures in the 450–500 °C range. On the other hand, note that the conversion attained over the pure silicas was lower than 5% at 500 °C.

Judging from the results included in Fig. 8 and Table 3, substantial differences in performance were clearly evident as a function of the selected hard template. The temperature required for 50% conversion varied between 270 and 295 °C, while 90% conversion was attained in the 315–345 °C range. It was found that the catalysts derived from the SBA-15 exhibited the best behaviour. By contrast, the sample prepared
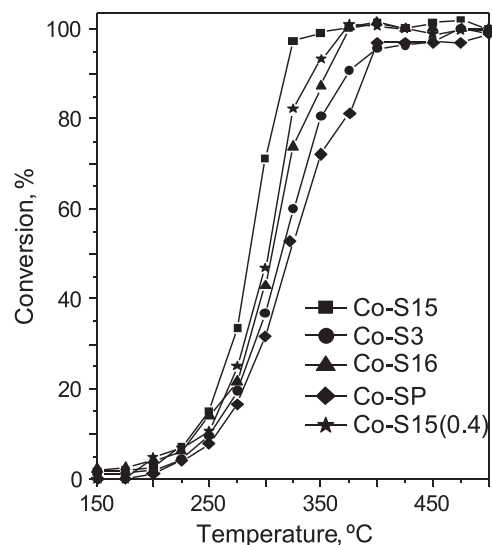

Fig. 8. Conversion of DCE to CO_2 over the hard-templated Co_3O_4 samples.

Table 3
Catalytic results of the oxidation of DCE over of the hard-templated Co_3O_4 samples.

| Catalyst	Areal reaction rate, $mmol\ m^{-2}\ h^{-1}$	T_{50}, °C	T_{90}, °C	S_{CO_2}, % (375 °C)	HCl/Cl_2 (375 °C)
Co-S15	0.260	285	320	100	1.3
Co-S3	0.213	315	375	95	1.0
Co-S16	0.224	305	355	97	0.8
Co-SP	0.125	320	390	92	0.8
Co-S15(0.4)	0.246	300	340	99	1.1

according to the SACOP method showed the poorest performance. Hence, the catalytic conversion, by considering the temperature for 50% conversion, followed this order: Co-S15 > Co-S15(0.4) > Co-S16 > Co-S3 > Co-SP. These results evidenced that the morphology of the catalysts played an important role for chlorinated VOC oxidation, being the 2D ordered nanorods more efficient than the wormhole-like samples. The observed high activity of nanocasted Co_3O_4 from SBA-15 was agreement with previous reports on the combustion of CO [28] and non-chlorinated VOCs such as benzene [29] and formaldehyde [30]. On the other hand, as for the more recent studies on the decomposition of DCE, Yang et al. [31,32] have profusely examined the behaviour of various Ce/Cr-based catalysts. When operating at a four times lower space velocity, a T_{50} value (with a selectivity to CO_2 higher than 90%) in the range 210–240 °C was attained, which was somewhat lower than that attained in this work.

Since the surface areas of the catalysts were considerably different, a more proper comparison of the intrinsic activity of the samples was made in terms of the areal reaction rate ($mmol_{DCE}\ m^{-2}\ h^{-1}$). This specific activity was calculated at 250 °C, where conversion of the feed to CO_2 was below 20% for all the samples (Table 3). The estimated values were between 0.26 and 0.12 $mmol_{DCE}\ m^{-2}\ h^{-1}$. Note that the activity trend was the same as that noticed as a function of the conversion vs temperature curves. Fig. 9 evidences that a good correlation existed between the specific activity and the proportion of Co^{2+} on the surface. As previously demonstrated, a high concentration in the surface of cobalt in low oxidation state (Co^{2+}) could be an indication of oxygen defects close to the surface. Hence, the presence of oxygen deficiencies, which was directly connected with a larger abundance of Co^{2+} ion on the surface, promoted the activation of gas-phase oxygen molecules for the generation of active oxygen species. This relatively large amount of oxygen vacancies in Co_3O_4 nanorods is usually associated with the existence of {220} crystal planes as catalytically active exposed planes [33,34]. Therefore, an attempt was made to identify the exposed planes of the Co-S15, Co-S16 and Co-S3 samples by HRTEM (Fig. 10). In all cases both {311} and {220} planes could be observed, with lattice fringes of 0.245 and 0.285 nm, respectively. In addition, the presence of less abundant {111} planes, with a lattice fringe of

0.466 nm, was also evident. On the basis of the analysis of 50–70 crystallites the relative abundance of these three planes could be roughly determined. Results depicted in Fig. 11 evidenced that the presence of {220} planes decreased in the following order: Co-S15(48%) > Co-S16(42%) > Co-S3(32%). This observed trend was in good agreement with the catalytic activity shown by the nanocasted Co_3O_4 catalysts. In sum, the notable catalytic performance of Co-S15 sample was related to its high oxygen adspecies concentrations and good low-temperature reducibility. These properties were in turn related to the existence of active {220} planes and a high population of Co^{2+} species at the surface, which ultimately were favoured by a relatively high surface area and a high quality 2D ordered mesoporous architecture [35–37]. On the other hand, the activity of the samples appeared to be also significantly influenced by the acid density, as revealed by the reasonably good correlation between the areal reaction rate and this property shown in Fig. S6 (supplementary material). This behaviour suggested that the mechanism of the reaction is controlled by the effective chemisorption of the chlorinated feed on an acid site and the subsequent attack of easily mobile oxygen species [38,39].

Ideally, a suitable catalyst must exhibit a high activity for DCE decomposition but also be selective towards CO_2, HCl and Cl_2 when the complete destruction of the feed ($> 95\%$) is achieved. Therefore, the presence of carbon monoxide and/or small amounts of partially oxidised hydrocarbons is not desirable. Hence, the product distribution of the hard-templated cobalt oxide catalysts was analysed. CO_2 selectivity was complete and no traces of CO were observed at any temperature. The negligible presence of CO as oxidation product was coherent with the results reported on the oxidation of hydrocarbons with varying chemical nature over Co_3O_4-based catalysts. It is noteworthy that this high selectivity to CO_2 instead of CO was found irrespective of the morphology and particle size of Co_3O_4 crystallites. Most of the investigations seem to favor a Mars-van Krevelen-type mechanism, which assumes surface oxygen ions of the Co_3O_4 catalyst participate in the CO oxidation as part of an overall reduction-oxidation cycle [40,41]. The most active sample (Co-S15) reached 100% CO_2 selectivity at 375 °C whereas the rest of the sample needed 400–425 °C, except for the Co-S3 sample, which required temperatures as high as 450 °C. These activity results contrasts with those obtained with other metal oxide catalysts, such as Mn_2O_3 and CeO_2, where significant amounts of carbon monoxide were obtained [42,43]. At lower reaction temperatures (< 350 °C), although no CO was noticed, small amounts of highly chlorinated byproducts such as vinyl chloride, carbon tetrachloride, tetrachloroethylene, trichloroethylene or dichloroethylene were detected. On the other hand, only HCl and Cl_2 as deep oxidation products at temperatures between 375 and 500 °C were detected. Table 3 includes the HCl/Cl_2 molar ratio at 375 °C. It varied between 1.3 for the Co-S15 sample and 0.8 for the Co-S16 and Co-SP oxides. The generation of large amounts of molecular chlorine was associated with the activity of Co_3O_4 in the Deacon reaction ($2HCl + \frac{1}{2}O_2 \leftrightarrow Cl_2 + H_2O$). The relative abundance of HCl/Cl_2 in the exit stream increased with temperature (from 400 to 500 °C), given that the equilibrium of the Deacon reaction was shifted towards HCl production.

Finally, attention was paid to examining the stability of the most active Co-S15 sample when operating at constant temperature during a relatively prolonged time on stream (120 h). An operation temperature of 325 °C (with a conversion well below 100%) was selected which was suitable for observing eventual changes of the catalyst performance. Results shown in Fig. 12 revealed a relatively stable conversion at about 90% and a selectivity to CO_2 close to 90%. A slight loss of activity occurred during the first reaction interval but the conversion remained roughly stable after operating for 20 h. The BET surface area decreased by about 20%, probably due to the accumulation of small amounts of carbonaceous by-products (2 wt.%) as revealed by XPS, and a slight sintering. The observed enlargement of the crystallite size (14%) could be attributed to hot spots on the surface of the catalyst during reaction. As for the presence of Cl species, both EDX and XPS analysis indicated
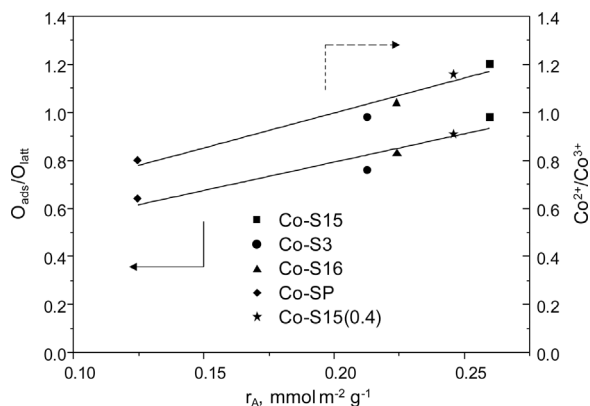
Fig. 9. Relationship of the areal reaction rate at 250 °C with the O_{ads}/O_{latt} ratio and the Co^{2+}/Co^{3+} ratio for the hard-templated Co_3O_4 samples.
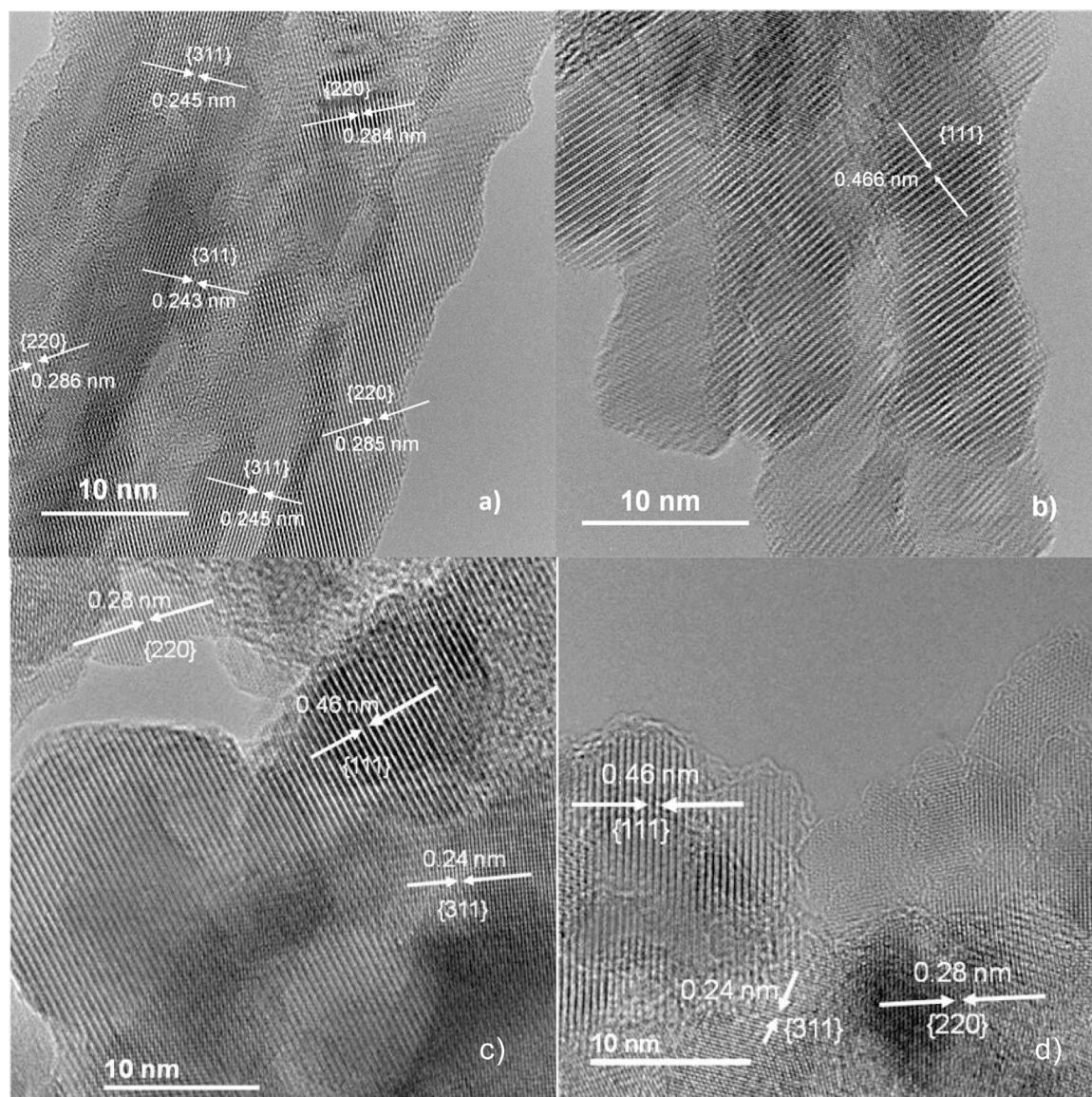
Fig. 10. HRTEM images of the hard-templated Co$_3$O$_4$ samples: a) and b) Co-S15, c) Co-S3, d) Co-S16.
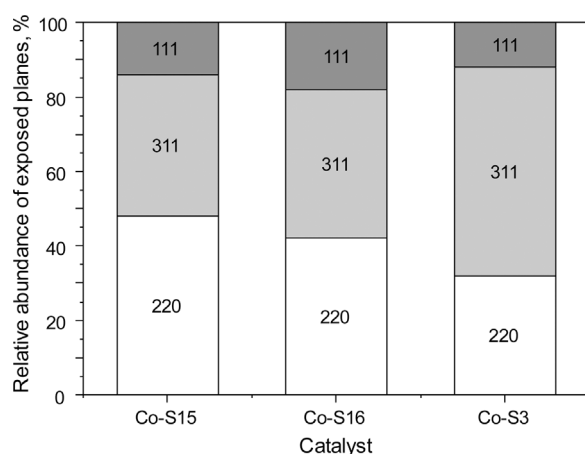

Fig. 11. Relative abundance of exposed planes (HRTEM) of the Co-S15, Co-S16 and Co-S3 samples.
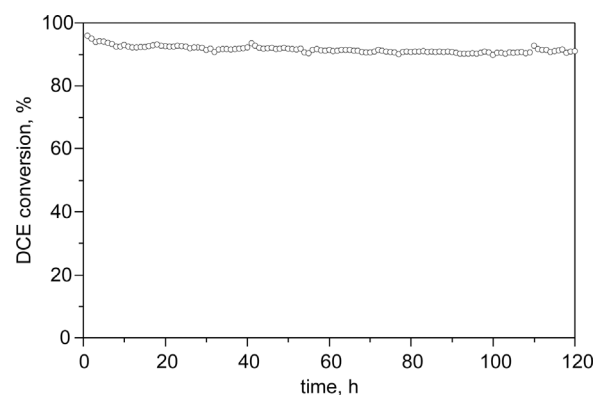

Fig. 12. Stability in DCE oxidation at 325 °C over the Co-S15 sample for 120 h.

the existence of small amounts of adsorbed Cl on the sample, about 1.5 wt.% and 4 wt.%, respectively. Furthermore, XPS results evidenced that the abundance of Co^{2+} and O$_{ads}$ species on the surface decreased with Co^{2+}/Co^{3+} and O$_{ads}$/O$_{latt}$ ratios of 1.1 and 0.9, respectively (1.2 and 1.0 for the fresh sample) (Fig. S7, supplementary material).

Interestingly, these minor changes did not seem to strongly influence the performance of the catalyst.

4. Conclusions

The use of hard-templating routes for the synthesis of bulk Co_3O_4 was highly promising for designing catalysts with improved physico-chemical properties for the oxidation of chlorinated compounds. Among the various mesoporous silica templates (SBA-15, SBA-16 and SBA-3), the catalyst obtained from SBA-15 was the most efficient in the oxidation of 1,2-dichloroethane.

The SBA-15 silica allowed for the preparation of a 2D ordered nanorod-like structure which was characterised by a relatively high surface area, high concentration of oxygen adspecies which was connected with an enrichment of Co^{2+} species at the surface and the existence of {220} crystal planes, and a good low-temperature reducibility. By contrast, the samples prepared from SBA-16 and SBA-3 and the catalyst obtained by silica aquagel confined precipitation exhibited a wormhole-like mesoporous structure that negatively influenced these key catalytic properties and the observed specific reaction rate. The nanocasted Co_3O_4 derived from the SBA-15 silica not only exhibited a high oxidation activity as temperatures as low as 350 °C with a notable selectivity to CO_2 and HCl/Cl_2 as main oxidation products were obtained, but also resulted very stable during prolonged reaction time intervals.

Acknowledgements

Appendix A. Supplementary data

Supplementary data associated with this article can be found, in the online version, at http://dx.doi.org/10.1016/j.apcatb.2017.09.050.

References

[1] E. Escalera, M.A. Ballem, J.M. Córdoba, M. Antti, M. Odén, Powder Technol. 221 (2012) 359–364.
[2] B. Solsona, T. García, R. Sanchis, M.D. Soriano, M. Moreno, E. Rodríguez−Castellón, S. Agouram, A. Dejoz, J.M. López Nieto, Chem. Eng. J. 290 (2016) 273–281.
[3] H. Gong, J. Zhu, K. Lv, P. Xiao, Y. Zhao, New. J. Chem. 39 (2015) 9380–9388.
[4] B. Solsona, T.E. Davies, T. Garcia, I. Vázquez, A. Dejoz, S.H. Taylor, Appl. Catal. B 84 (2008) 176–184.
[5] T. Garcia, S. Agouram, J.F. Sánchez−Royo, R. Murillo, A.M. Mastral, A. Aranda, I. Vázquez, A. Dejoz, B. Solsona, Appl. Catal. A 386 (2010) 16–27.
[6] J. Zhu, Q. Gao, Micropor. Mesopor Mater. 124 (2009) 144–152.
[7] Y. Ren, Z. Ma, P.G. Bruce, Chem. Soc. Rev. 41 (2012) 4909–4927.
[8] D. Gu, F. Schüth, Chem. Soc. Rev. 43 (2014) 313–344.
[9] J. González-Prior, J.I. Gutiérrez-Ortiz, R. López-Fonseca, G. Busca, E. Finocchio, B. de Rivas, Catal. Sci. Technol. 6 (2016) 5618–5630.
[10] O. González, H. Pérez, P. Navarro, L.C. Almeida, J.G. Pacheco, M. Montes, Catal. Today. 148 (2009) 140–147.
[11] M. Mesa, L. Sierra, J.- Guth, Micropor. Mesopor. Mater. 112 (2008) 338–350.
[12] I. López, T. Valdés-Solís, G. Marbán, ChemCatChem 3 (2011) 734–740.
[13] J. González-Prior, R. López-Fonseca, J.I. Gutiérrez-Ortiz, B. de Rivas, Appl. Catal. B 199 (2016) 384–393.
[14] A. Feliczak-Guzik, B. Jadach, H. Piotrowska, M. Murias, J. Lulek, I. Nowak, Micropor. Mesopor. Mater. 220 (2016) 231–238.
[15] P.I. Ravikovitch, A.V. Neimark, J. Phys. Chem. B 105 (2001) 6817–6823.
[16] M.V. Ponte, L.P. Rivoira, J. Cussa, M.L. Martínez, A.R. Beltramone, O.A. Anunziata, Micropor. Mesopor. Mater. 227 (2016) 9–15.
[17] E. Rombi, M.G. Cutrufello, L. Atzori, R. Monaci, A. Ardu, D. Gazzoli, P. Deiana, I. Ferino, Appl Catal A Gen. 515 (2016) 144–153.
[18] P. Djinovic, J. Batista, J. Levec, A. Pintar, Appl. Catal. A 364 (2009) 156–165.
[19] S. Zuo, F. Liu, J. Tong, C. Qi, Appl. Catal. A 467 (2013) 1–6.
[20] Y. Du, Q. Meng, J. Wang, J. Yan, H. Fan, Y. Liu, H. Dai, Micropor. Mesopor. Mater. 162 (2012) 199–206.
[21] S.A. Singh, G. Madras, Appl. Catal. A 504 (2015) 463–475.
[22] C. Liu, Q. Liu, L. Bai, A. Dong, G. Liu, S. Wen, J. Mol. Catal. A 370 (2013) 1–6.
[23] X. Zhang, P. Zhang, H. Yu, Z. Ma, S. Zhou, Catal. Lett. 145 (2015) 784–793.
[24] M. Králik, Z. Vallušová, P. Major, A. Takácová, M. Hronec, D. Gašparovicová, Chem. Pap. 68 (2014) 1690–1700.
[25] G. Bai, H. Dai, J. Deng, Y. Liu, F. Wang, Z. Zhao, W. Qiu, C.T. Au, Appl. Catal. A 450 (2013) 42–49.
[26] S. Esposito, A. Setaro, P. Maddalena, A. Aronne, P. Pernice, M. Laracca, J. Sol-Gel Sci. Technol. 60 (2011) 388–394.
[27] K. Shojaee, B.S. Haynes, A. Montoya, Proc. Combust. Inst. 36 (2017) 4365–4373.
[28] Y. Zhang, A. Wang, Y. Huang, Q. Xu, J. Yin, T. Zhang, Catal. Lett. 142 (2012) 275–281.
[29] C. Ma, Z. Mu, C. He, P. Li, J. Pi, Z. Hao, J. Environ. Sci. 23 (2011) 2078–2086.
[30] B. Bai, H. Arandiyan, J. Li, Appl. Catal. B 142-143 (2013) 677–683.
[31] P. Yang, S. Zuo, Z. Shi, F. Tao, R. Zhou, Appl. Catal. B 191 (2016) 53–61.
[32] P. Yang, S. Zuo, R. Zhou, J. Chem. Eng. 323 (2017) 160–170.
[33] J. Yongchang, W. Shuyuan, L. Jiqing, L. Mengfei, Chem. Res. Chin. Univ. 32 (2016) 808–811.
[34] W.J. Xue, Y.F. Wang, P. Li, Z.-T. Liu, Z.P. Hao, C.Y. Ma, Catal. Commun. 12 (2011) 1256–1268.
[35] L.F. Liotta, M. Ousmane, G. Di Carlo, G. Pantaleo, G. Deganello, G. Marcì, L. Retailleau, A. Giroir-Fendler, Appl. Catal. A 347 (2008) 81–88.
[36] J. Taghavimoghaddam, G.P. Knowles, A.L. Chaffee, J. Mol. Catal. A 358 (2012) 79–88.
[37] H. Song, U.S. Ozkan, J. Catal. 261 (2009) 66–74.
[38] R. López-Fonseca, B. de Rivas, J.I. Gutiérrez-Ortiz, A. Aranzabal, J.R. González-Velasco, Appl. Catal. B 41 (2003) 31–42.
[39] B. de Rivas, C. Sampedro, M. García-Real, R. López-Fonseca, J.I. Gutiérrez-Ortiz, Appl. Catal. B 129 (2013) 225–235.
[40] P. Broqvist, I. Panas, H. Persson, J. Catal. 201 (2002) 198–206.
[41] S. Sun, Q. Gao, H. Wang, J. Zhu, H. Guo, Appl. Catal. B 97 (2010) 284–291.
[42] B. de Rivas, C. Sampedro, E.V. Ramos-Fernández, R. López-Fonseca, J. Gascon, M. Makkee, J.I. Gutiérrez-Ortiz, Appl. Catal. A 456 (2013) 96–104.
[43] J.I. Gutiérrez-Ortiz, R. López-Fonseca, U. Aurrekoetxea, J.R. González-Velasco, J. Catal. 218 (2003) 148–154.